

## Influence of laser beam profile on electromagnetically induced absorption

S. M. Ćuk, M. Radonjić, A. J. Krmpot,\* S. N. Nikolić, Z. D. Grujić, and B. M. Jelenković  
*Institute of Physics, University of Belgrade, Pregrevica 118, 11080 Belgrade, Serbia*

(Received 25 August 2010; published 1 December 2010)

We compared, experimentally and theoretically, Hanle electromagnetically induced absorption (EIA) obtained using Gaussian and  $\Pi$ -shaped laser beams 3 mm in diameter. The study was done by measuring the transmission of a laser locked to the  $F_g = 2 \rightarrow F_e = 3$  transition at the  $D_2$  line of  $^{87}\text{Rb}$  in a vacuum cell. EIA linewidths obtained for the two laser profiles were significantly different in the range of laser intensities 1–4 mW/cm<sup>2</sup>. EIA with the  $\Pi$ -shaped laser beam has a broad intensity maximum and linewidths larger than those obtained with the Gaussian beam profile. We also studied Hanle EIA by measuring the transmission of selected segments of the entire laser beam by placing a small movable aperture in front of the detector. Waveforms so obtained in Hanle EIA resonances were strongly influenced both by the radial distance of the transmitted segment from the beam center and by the radial profile of the laser beam. We show that outer regions of Gaussian beam, and central regions of the  $\Pi$ -shaped beam generate the narrowest lines. The different behaviors of EIA owing to different beam profiles revealed by both theory and experiment indicate the importance of the radial profile of the laser beam for proper modeling of coherent effects in alkali metal vapors.

DOI: [10.1103/PhysRevA.82.063802](https://doi.org/10.1103/PhysRevA.82.063802)

PACS number(s): 42.50.Gy, 42.50.Nn, 42.62.Fi, 42.65.–k

### I. INTRODUCTION

Coherent phenomena in Doppler broadened alkali metal atom vapors have been thoroughly examined over the past decade. Coherent population trapping (CPT) [1,2], electromagnetically induced transparency (EIT) [3], and electromagnetically induced absorption (EIA) [4,5] have been observed and analyzed in either a pump-probe or a Hanle configuration [6,7]. EIA is observed in so-called  $V$  atomic schemes, such that  $F_g \rightarrow F_e = F_g + 1$ , and  $F_g > 0$ , where  $F_{g,e}$  are total angular momenta of the ground and excited states, respectively [8]. This phenomenon is a consequence of the transfer of coherence and the transfer of population due to spontaneous emission between the excited and the ground degenerate states [9,10]. Due to coherences developed between Zeeman sublevels, EIA could have an important role in sub-Doppler and subrecoil laser cooling mechanisms [11].

All phenomena mentioned strongly depend on the intensity of the applied laser field. Laser intensity dependence of CPT and EIT lineshapes has been studied extensively. It is shown that EIT linewidths have a linear dependence on the laser electric field at lower intensities and a linear dependence on laser intensity at higher intensities [12–14]. The EIA linewidth, in contrast, seems to have a maximum near the saturation limit [15].

The term “laser intensity” is ordinarily used in the sense of an average beam intensity (laser power divided by beam area), regardless of the laser beam profile used in the study. Since coherent phenomena are generally nonlinear, they depend strongly not only on the total beam intensity but also on the radial intensity distribution of the used laser. The typical laser beam profile used in experiments is Gaussian. Theoretical descriptions commonly assume a  $\Pi$ -shaped beam profile. The influence of different laser beam profiles has been studied only for EIT lineshapes in a few papers [16–18].

The goal of the present paper is to give a comparative study of the Hanle EIA resonances obtained with two radial laser

beam profiles, Gaussian and  $\Pi$ -shaped. Our investigation was performed on  $^{87}\text{Rb}$  vapor in a vacuum cell at the  $D_2$  line in the Hanle configuration. This simple configuration requires only a single laser and a scanning external magnetic field, oriented parallel to the laser propagation direction. We studied EIA obtained from two beam profiles by detecting the entire 3-mm-diameter laser beam and, also, by detecting light coming from small cylindrical volumes selected by the movable 0.5-mm aperture in front of the detector. For low intensities of light passing through the aperture, the selected cylindrical volume, which we denote as quasiprobe region, plays the role of a typical probe beam. The rest of the laser beam is considered to be the pump supplying coherently prepared atoms to the quasiprobe region. Thus, we call the Hanle configuration with the movable aperture the quasiprobe Hanle configuration. Studies of EIA from selected parts of the laser beam were done by moving the aperture along the laser beam radius. Similar measurements for EIT have recently demonstrated the essential influence of different parts of the Gaussian laser beam on the overall EIT resonances, that is, on the EIT from the whole laser beam [19,20]. Our theoretical model gives the Hanle resonance lineshapes in accordance with measurements. Calculations are based on the optical Bloch equations for transient evolution of the atomic state during interaction with laser light of a profiled intensity. The effects of light propagation through polarized atomic vapor are included in the theoretical description.

### II. EXPERIMENT

The experimental setup is shown in Fig. 1(a). The external-cavity diode laser is frequency locked to the  $F_g = 2 \rightarrow F_e = 3$  transition at the  $D_2$  line in  $^{87}\text{Rb}$ , where  $F_g$  and  $F_e$  represent the angular momenta of the ground- and excited-state hyperfine levels, respectively. Laser locking is performed in an auxiliary vacuum Rb cell using the Doppler-free dichroic atomic vapor laser lock (DDAVLL) method [21]. The variable neutral density filter is used for laser power adjustments. Single-mode fiber was used to provide the Gaussian laser beam. After passing through the Glan-Thompson polarizer, the laser beam becomes linearly polarized.

\*krmpot@ipb.ac.rs

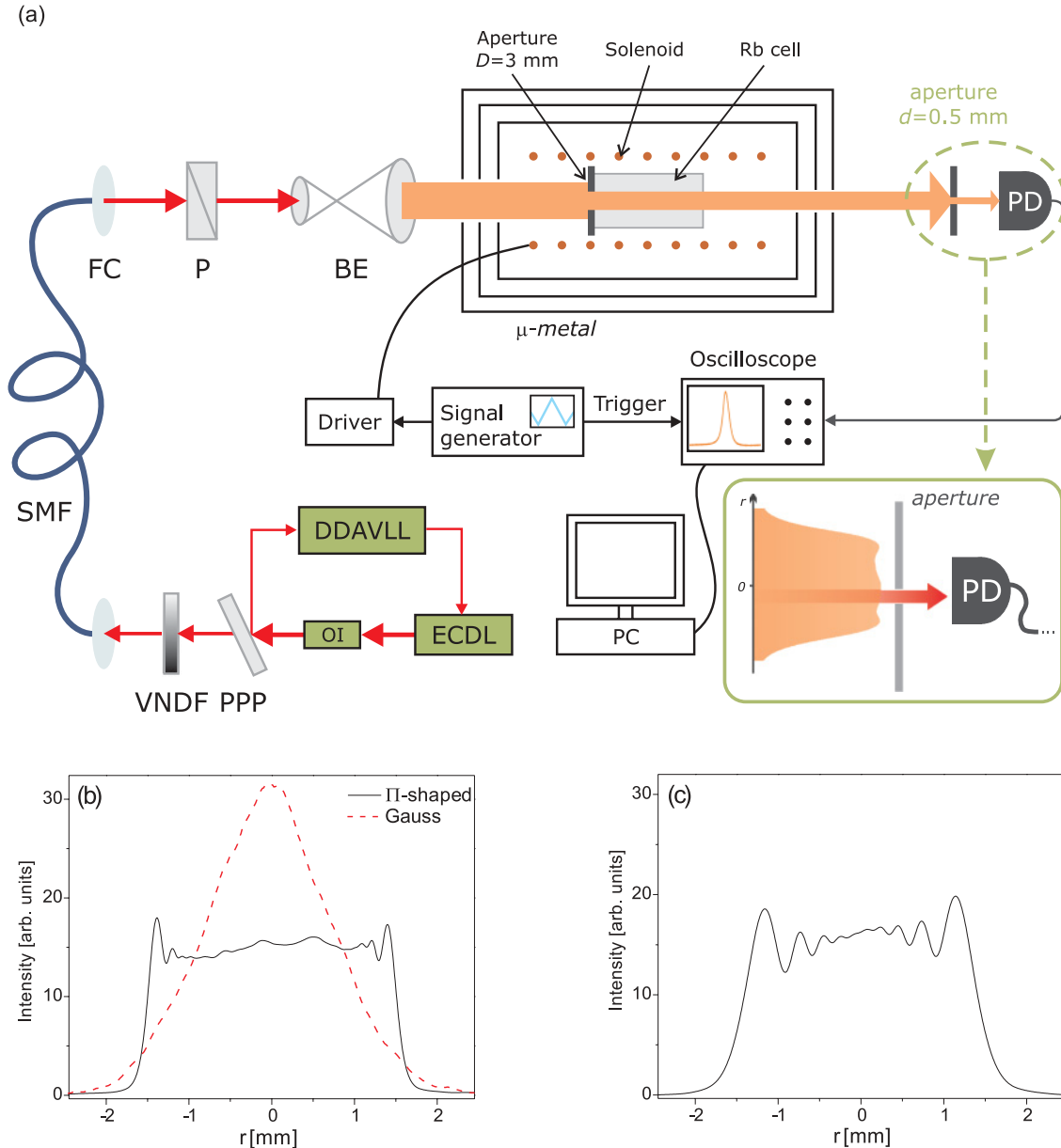


FIG. 1. (Color online) (a) Experimental setup: ECDL, external cavity diode laser; OI, optical isolator; DDAVLL, Doppler-free dichroic atomic vapor laser lock; VNUDF, variable neutral density filter; SMF, single-mode fiber; FC, fiber collimator; P, polarizer; BE, beam expander; PD, photodiode. Moving the aperture on the translation stage allows only a selected part of the laser beam to reach the detector, while the rest of the laser beam is blocked.  $\Pi$ -shaped beam profiles were recorded by a beam profiler placed at 3 cm (b) and 30 cm (c) from the 3-mm circular aperture. (b) The dashed (red) curve is the profile of a Gaussian laser beam of the same power and diameter as the  $\Pi$ -shaped beam.

For experiments with the Gaussian profile, the laser beam is expanded to 3 mm in diameter. Laser beam diameters are determined from the  $1/e^2$  value. The  $\Pi$ -shaped laser beam profile was obtained after expanding the Gaussian laser beam to 20 mm in diameter and then extracting its central part via the circular aperture placed on the entrance window of the cell. Diffraction affects the beam shape in the Rb cell and one has to settle for an approximation of the  $\Pi$  shape of the laser beam. After experimenting with different diameters of the expanded Gaussian laser beam, sizes of apertures, and thicknesses of the foil used for the apertures, we obtained the  $\Pi$ -shaped laser beam whose radial intensity profiles are given in Figs. 1(b) and 1(c). The beam profiles measured by the beam profiler are 3 and 30 cm away from the 3-mm aperture on 0.1-mm tick foil.

The first profile is at a distance equal to the distance between the aperture and the mid section of the Rb cell. This profile is referred to as  $\Pi$ -shaped throughout the paper. We used the beam profile at 30 cm from the aperture to show relatively small changes in the profile with distance and to justify use of the  $\Pi$ -shaped profile in the theoretical model. Together with the  $\Pi$ -shaped laser beam profile, the profile of the Gaussian laser beam is also given in Fig. 1(b). The two beams whose profiles are shown there have the same power and the same diameter.

The laser beam passes through the 6-cm-long vacuum Rb cell containing a natural abundance of rubidium isotopes. The cell is placed in the solenoid used for scanning the axial magnetic field between  $-50$  and  $+50$   $\mu\text{T}$ . The cell and the solenoid are placed inside triple-layered  $\mu$ -metal cylinders

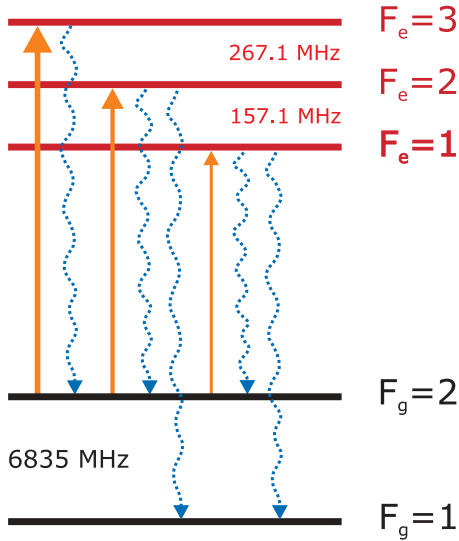


FIG. 2. (Color online) Energy level diagram for  $D_2$  line transitions considered in the theoretical model. Solid lines represent transitions induced by the laser, while dotted lines correspond to possible spontaneous emission channels from excited levels. Frequency differences between adjacent hyperfine levels are shown.

to eliminate Earth's and stray magnetic fields. In the part of the experiment studying the effects of the laser beam profile on the intensity dependence of whole-laser-beam EIA, the entire transmitted laser beam was detected while scanning the external magnetic field.

To measure Hanle EIA from only small parts of the laser beam, a movable aperture 0.5 mm in diameter is placed in front of the large detection surface photodiode (area, 80 mm<sup>2</sup>). By moving the aperture with the fine translation stage we allow only light from a small segment of transmitted laser beam to reach the photodiode. The signal obtained from this photodiode while scanning the external magnetic field is recorded by the digital oscilloscope and transferred to the computer.

### III. THEORETICAL MODEL

Hanle EIA resonances were calculated for the  $D_2$  line transition  $F_g = 2 \rightarrow F_e = 3$  of  $^{87}\text{Rb}$  coupled to a linearly polarized laser in a Rb vacuum cell. The energy level diagram given in Fig. 2 shows hyperfine levels either coupled to the laser light or populated due to spontaneous emission. The quantization  $z$  axis is chosen to be parallel to the external magnetic field. The complete magnetic sublevel structure is taken into account in calculations. The model is based on time-dependent optical Bloch equations for the density matrix of a moving atom,

$$\frac{d\rho}{dt} = -\frac{i}{\hbar}[H_{\text{atom}}(B) + H_{\text{int}}(t), \rho] + \left(\frac{d\rho}{dt}\right)_{\text{SE}}, \quad (1)$$

where

$$H_{\text{atom}}(B) = \sum_j \hbar\omega_j(B)|g_j\rangle\langle g_j| + \sum_k \hbar\omega_k(B)|e_k\rangle\langle e_k| \quad (2)$$

is the atomic Hamiltonian corresponding to the ground (excited) states  $|g_j\rangle$  ( $|e_k\rangle$ ) with Zeeman-shifted energies  $\hbar\omega_j(B)$  [ $\hbar\omega_k(B)$ ] in the external magnetic field  $B$ . Laser-atom

interaction is given by

$$H_{\text{int}}(t) = -\sum_{j,k} \mathbf{E}(t) \cdot \mathbf{d}_{jk}(|g_j\rangle\langle e_k| + |e_k\rangle\langle g_j|), \quad (3)$$

where  $\mathbf{E}(t)$  is the time-dependent laser electrical field and  $\mathbf{d}_{jk}$  is the atomic electric dipole moment for the transition between state  $|g_j\rangle$  and state  $|e_k\rangle$ . Spontaneous emission is included through the Lindblad-form term,

$$\left(\frac{d\rho}{dt}\right)_{\text{SE}} = \sum_m 2\Gamma_m \rho \Gamma_m^\dagger - \Gamma_m^\dagger \Gamma_m \rho - \Gamma_m \Gamma_m^\dagger \rho, \quad (4)$$

where  $\Gamma_m$  are operators corresponding to dipole transitions from the excited- to the ground-state manifold. Although the laser is frequency locked to the  $F_g = 2 \rightarrow F_e = 3$  transition, owing to the Doppler broadening, the excited hyperfine levels  $F_e = 2$  and  $F_e = 1$  are also laser coupled and taken into consideration. Equations for density matrix elements related to the  $F_g = 1$  ground level are excluded since that level is not coupled by the laser. For additional details about the resulting equations please refer to [18]. It is assumed that after colliding with cell walls, atoms reset into the internal state with equally populated ground magnetic sublevels. Between collisions with cell walls, rubidium atoms interact only with an axially oriented homogeneous magnetic field and spatially dependent laser electric field. Collisions among Rb atoms are negligible due to low Rb vapor pressure at room temperature so that an atom moves through the laser beam at a constant velocity  $\mathbf{v} = \mathbf{v}_{\parallel} + \mathbf{v}_{\perp}$ , where  $\mathbf{v}_{\parallel}$  and  $\mathbf{v}_{\perp}$  are velocity components parallel and perpendicular to the laser propagation direction, respectively. The former affects the longitudinal direction of the atomic trajectory and Doppler shift of the laser frequency seen by a moving atom, while the latter determines the transverse direction of the trajectory and the interaction time.

The dependence of the laser intensity on the radial distance  $r$  for the Gaussian profile is

$$I(r) = 2\bar{I} \exp(-2r^2/r_0^2), \quad (5)$$

where  $r_0$  is  $1/e^2$  beam radius and  $\bar{I}$  is the beam intensity (total laser power divided by  $r_0^2\pi$ ). A  $\Pi$ -shaped profile of the same intensity and radius was modeled using the equation

$$I(r) = \bar{I}a \{1 + \text{erf}[p(r_0 - r)]\}^2, \quad (6)$$

where  $a$  is the normalization constant and  $p$  is a positive parameter affecting the steepness of the profile near  $r = r_0$ . In our calculations we neglect longitudinal changes in the beam profile compared to transverse ones, so that only the transverse direction of the trajectory matters. Therefore, we drop the explicit dependence on  $z$  of all physical quantities. From the reference frame of the moving atom, the electric field varies and the rate of variation depends only on  $\mathbf{v}_{\perp}$ . Assume that the transverse projection of the atomic trajectory is given by  $\mathbf{r}_{\perp}(t) = \mathbf{r}_{0\perp} + \mathbf{v}_{\perp}t$ , where  $\mathbf{r}_{0\perp}$  is the perpendicular component of the atom position vector at  $t = 0$ . The temporal variation of the laser intensity seen by the atom is given by

$$I(t) \equiv I(\mathbf{r}_{\perp}(t)) = I(\mathbf{r}_{0\perp} + \mathbf{v}_{\perp}t), \quad (7)$$

representing the spatial laser intensity variation along the trajectory of the atom in the laboratory frame. Additionally, due to the cylindrical symmetry of the beam profile, spatial dependence becomes purely radial dependence.

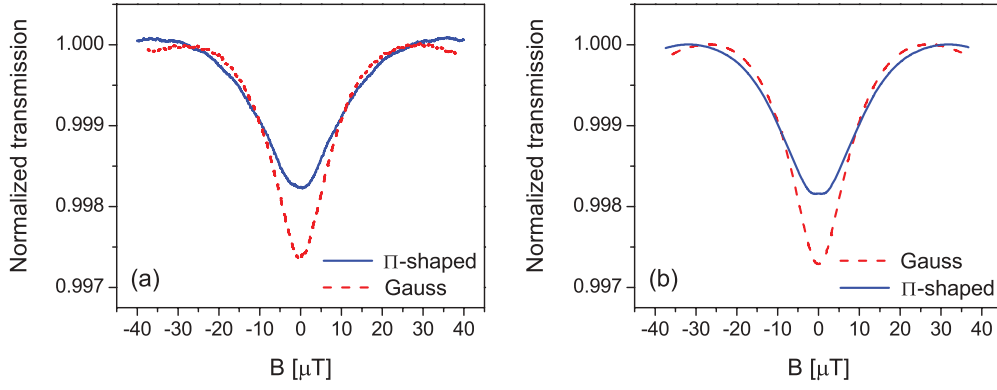


FIG. 3. (Color online) Experimental (a) and theoretical (b) Hanle EIA resonances for the Gaussian [dashed (red) curves] and  $\Pi$ -shaped [solid (blue) curves] beam profiles. Laser intensity is  $2 \text{ mW/cm}^2$ .

The observed resonances in EIA experiments are the probabilistic average of contributions due to many individual, mutually noninteracting atoms. Rb atoms traverse the laser beam at different paths with different velocities. The Maxwellian velocity distribution, diversity of atomic trajectories, and custom cylindrically symmetric radial profile of the laser electric field are treated similarly as in [18]. Trajectories at different distances from the laser beam center are chosen so that the beam cross section is uniformly covered. For a representative set of atomic velocities the atomic density matrix  $\rho(B; \mathbf{v}; \mathbf{r}_\perp)$  along a given trajectory is calculated assuming a constant magnetic field  $B$  during the atomic transit through the laser beam. To obtain the atomic ensemble density matrix  $\rho(B; r)$  across the beam cross section for a set of radial distances  $r$ , the calculated density matrices are averaged over the Maxwell-Boltzmann velocity distribution and integrated over trajectories containing points at a given radial distance  $r$ . Owing to the cylindrical symmetry of the laser beam profile and the atomic velocity distribution, the velocity-averaged density matrix will also be cylindrically symmetric. Thus, the angular integral appearing in the averaging over velocity  $\mathbf{v}(\theta) = (\theta, v_\perp, v_\parallel)$  can be replaced with an angular integral over space

$$\rho(B; r) = \int_0^{2\pi} \frac{d\theta}{2\pi} \int_0^\infty dv_\perp W_\perp(v_\perp) \times \int_{-\infty}^\infty dv_\parallel W_\parallel(v_\parallel) \rho(B; 0, v_\perp, v_\parallel; r \cos \theta, r \sin \theta), \quad (8)$$

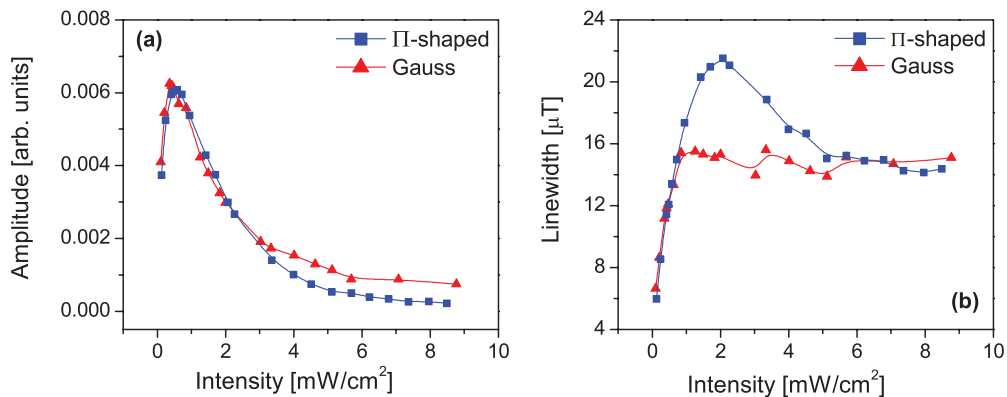


FIG. 4. (Color online) Experimental (a) amplitudes and (b) linewidths for Gaussian [(red) triangles] and  $\Pi$ -shaped [(blue) squares] beam profiles as a function of the laser intensity.

with the Maxwell-Boltzmann velocity distribution given by

$$W_\perp(v_\perp) = \frac{2v_\perp}{u^2} e^{-(v_\perp/u)^2}, \quad (9a)$$

$$W_\parallel(v_\parallel) = \frac{1}{u\sqrt{\pi}} e^{-(v_\parallel/u)^2}, \quad (9b)$$

where  $u = (2k_B T/m_{\text{Rb}})^{1/2}$  is the most probable velocity.

The effects of the laser propagation along the cell and induced atomic polarization of the Rb vapor are included using the following approximations. We first compute the Rb vapor ensemble density matrix  $\rho(B; r)$  and polarization  $\mathbf{P}$  assuming a constant value of the electric field  $\mathbf{E}$  along the  $z$  direction of laser propagation within the cell. The polarization of Rb vapor is obtained from the ensemble density matrix,

$$\mathbf{P}(B; r) = n(T) \text{Tr}[\rho(B; r) \mathbf{e}\hat{\mathbf{r}}], \quad (10)$$

where the  $^{87}\text{Rb}$  concentration at temperature  $T$  is given by [22]

$$n(T) = 0.2783 \times \frac{133.322}{k_B T} \times 10^{-94.0483 - 0.0377169T - 1961.26/T + 18.4902 \log_{10}(T)}. \quad (11)$$

Due to trace operations including dipole operator  $\mathbf{e}\hat{\mathbf{r}}$ , the polarization  $\mathbf{P}$  depends only on the optical coherences between the ground and the excited Zeeman sublevels. Using the computed Rb polarization, we calculate the change of the electric field due to propagation of the laser through the Rb

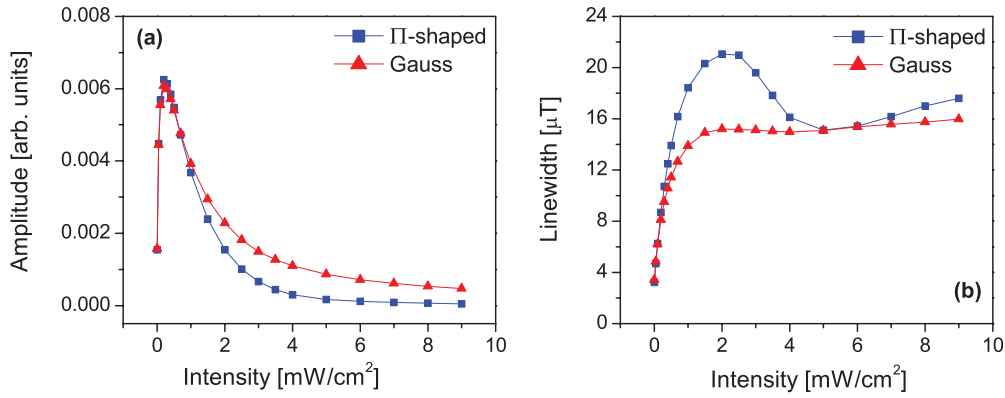


FIG. 5. (Color online) Theoretical (a) amplitudes and (b) linewidths for Gaussian [(red) triangles] and  $\Pi$ -shaped [(blue) squares] beam profiles as a function of the laser intensity.

vapor. Assuming that the change of electric field along the length  $L$  of the Rb cell is small enough, the exact relation

$$\frac{\partial \mathbf{E}(B; r, z)}{\partial z} = \frac{i\omega_0}{2\epsilon_0 c} \mathbf{P}(B; r, z) \quad (12)$$

in the first approximation takes the form

$$\mathbf{E}(B; r, z = L) = \mathbf{E}(B; r, z = 0) + \frac{i\omega_0}{2\epsilon_0 c} \mathbf{P}(B; r)L, \quad (13)$$

where  $\epsilon_0$  is the vacuum dielectric constant and  $\omega_0$  is the laser frequency. The transmitted electric field of Eq. (13) is used in the calculations of Hanle EIA resonances. The cell temperature was set to 25°C as in experiments.

#### IV. RESULTS AND DISCUSSION

Figure 3 shows a comparison of Hanle EIA resonances for Gaussian and  $\Pi$ -shaped profiles, at a laser intensity of 2 mW/cm<sup>2</sup>. The quoted laser intensity corresponds to the intensity of the whole laser beam, that is, the measured laser power at the entrance of the cell divided by the beam area. Figure 3(a) corresponds to experiment and Fig. 3(b) shows theoretical results. Key features of any resonance are amplitude and linewidth. It can be seen that for an intensity of 2 mW/cm<sup>2</sup>, the  $\Pi$ -shaped beam profile yields resonances with

a greater linewidth. Figure 4 presents experimental, and Fig. 5 theoretical, results for the amplitudes and linewidths of EIA resonances as a function of the laser intensity, for both laser profiles. EIA amplitudes are normalized to transmitted laser intensity. In each figure we give results obtained using two radial laser beam profiles. It is shown that amplitude intensity dependencies for both profiles initially rise quite rapidly, until they reach a maximum at approximately 0.5 mW/cm<sup>2</sup>. Further decrease with the laser intensity is a consequence of saturation.

Resonance linewidths obtained from the two beam profiles have different dependences on the laser intensity. For both beam profiles there is a very rapid increase at low intensities. However, the  $\Pi$ -shaped profile gives a pronounced maximum at about 2 mW/cm<sup>2</sup>, while the Gaussian profile provides an almost-flat linewidth dependence at these and higher intensities. EIA intensity narrowing at high laser intensities, assuming a  $\Pi$ -shaped beam, was noted earlier, in [15]. Differences in linewidths are most notable for moderate intensities and are due to different transient dynamics of atoms passing through the laser beam. During atomic transit through the laser beam the atomic state changes due to competitive effects of the laser excitation and the external magnetic field. The laser continuously forces the atom to be “aligned” with the electric field, in which case the state of the atom relates to the appearance of EIA. The external magnetic field causes oscillations

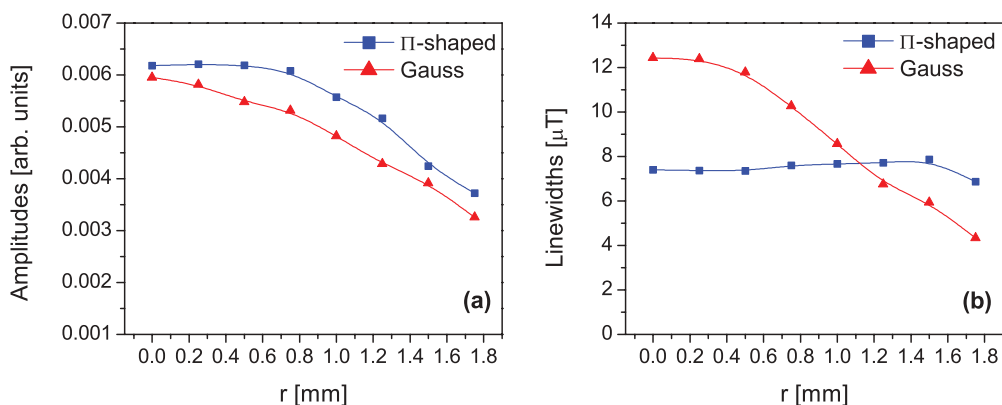


FIG. 6. (Color online) Experimental results for (a) amplitude and (b) linewidth of EIA obtained from laser beam sections at different radial distances from the laser beam center for Gaussian [(red) triangles] and  $\Pi$ -shaped [(blue) squares] beam profiles. Points correspond to different radial distances of the 0.5-mm aperture selecting the sections. Laser intensity is 0.2 mW/cm<sup>2</sup>.

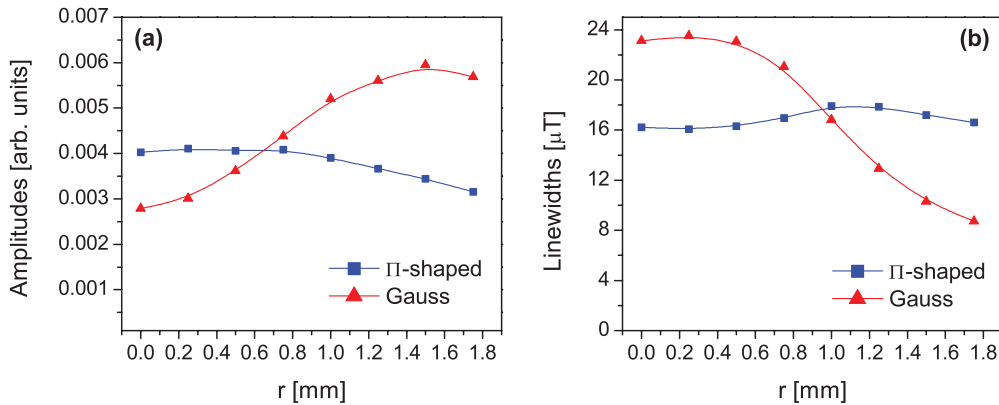


FIG. 7. (Color online) Experimental results for (a) amplitude and (b) linewidth EIA dependence on the radial position of the 0.5-mm aperture for Gaussian [(red) triangles] and  $\Pi$ -shaped [(blue) squares] beam profiles. Laser intensity is  $1 \text{ mW/cm}^2$ .

of the atomic state at the corresponding Larmor frequency. At low laser intensities, the influence of the magnetic field is more significant, so that the atomic state “aligned” with the electric field is degraded more easily. For the Gaussian laser beam, the atoms experience an omnichanging laser field, while the  $\Pi$ -shaped beam provides an almost-constant electric field. This difference reflects directly on the robustness of the “aligned” atomic state with respect to the external magnetic field because the spatial change in the laser field decreases the robustness by inducing an extra variation of the atomic state. Under a zero external magnetic field atoms reach an “aligned” state, and absorption reaches a maximum. A nonzero magnetic field degrades that state, reducing the absorption. If the “aligned” state is more robust, the absorption decreases less for the same magnetic field. Therefore, greater robustness of the EIA with respect to the external magnetic field requires a larger magnetic field to halve the peak absorption and hence yields larger EIA linewidths for the  $\Pi$ -shaped beam, compared to the Gaussian beam. When the laser intensity is high enough, differences in laser beam profile become less important, yielding very similar linewidths for both profiles.

We also studied Hanle EIA obtained by detecting transmitted light from only a part of the laser beam, as a function of the magnetic field. This was done, as explained in Sec. I, by placing a 0.5-mm aperture between the Rb cell and the detector.

We then effectively measure EIA from the cylindrical volume of the medium, which is surrounded by the same medium, illuminated by the same laser. We can regard this as a quasi probe-pump configuration, where the probe is surrounded by a copropagating pump. In such quasiprobe Hanle EIA, resonances are either because of EIA atoms coming into the probe from the surrounding pump area or because of EIA induced by the probe. Relative contributions of the probed and induced part of the observed EIA depend on the overall laser intensity, shape of the beam (Gaussian or  $\Pi$ -shaped), and radial distance of the quasiprobe with respect to the laser beam center.

Figures 6 and 7 present measurement results for amplitudes [Figs. 6(a) and 7(a)] and linewidths [Figs. 6(b) and 7(b)] of Hanle quasiprobe EIA resonances as a function of radial positions of the selected beam segment, at a laser intensity of 0.2 and  $1 \text{ mW/cm}^2$ , respectively. Figures 8 and 9 are corresponding theoretical results. While quasiprobe linewidths for the  $\Pi$ -shaped profile are largest at the outer parts of the laser beam, linewidths for the Gaussian laser beam are larger near the laser beam center. This can be attributed to the fact that in the region near the beam boundary, the  $\Pi$ -shaped profile has a higher intensity than the Gaussian. The intensity inside the Gaussian beam increases constantly toward the beam center, causing EIA resonance broadening, so the situation reverses around the radial distance where the Gaussian beam becomes more intense (note that it is two times more intense at the

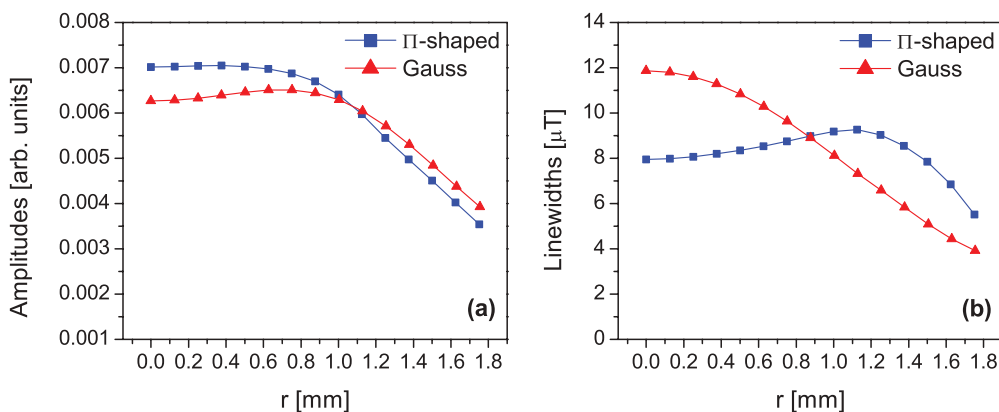


FIG. 8. (Color online) Theoretical results for (a) amplitude and (b) linewidth as a function of the radial position of the 0.5-mm aperture for Gaussian [(red) triangles] and  $\Pi$ -shaped [(blue) squares] beam profiles. Laser intensity is  $0.2 \text{ mW/cm}^2$ .

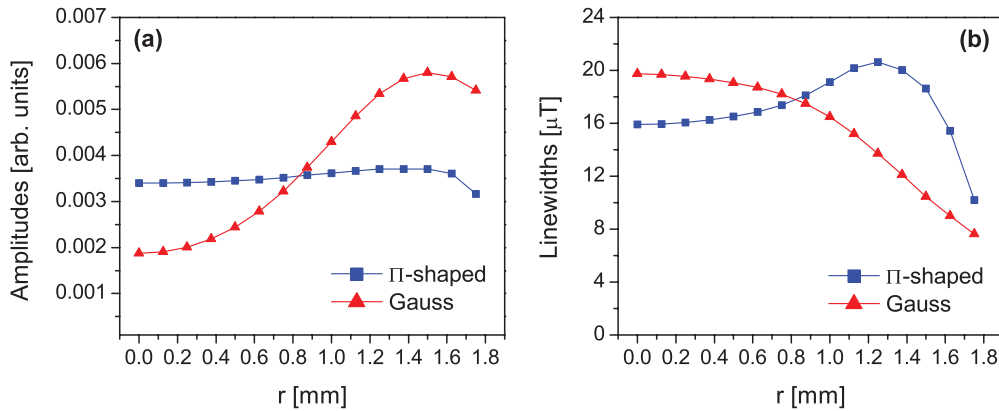


FIG. 9. (Color online) Theoretical results for (a) amplitude and (b) linewidth dependence on the radial position of the 0.5-mm aperture determining the beam segment for Gaussian [(red) triangles] and  $\Pi$ -shaped [(blue) squares] beam profiles. Laser intensity is  $1 \text{ mW/cm}^2$ .

center than the  $\Pi$ -shaped beam). Note that EIA resonances are particularly narrow in the wings of the Gaussian beam, where a very low intensity quasiprobe really probes the “aligned” EIA state of the atoms coming into the quasiprobe from the rest of the beam. At places closer to the beam center, the quasiprobe simultaneously probes and induces EIA, and eventually the induced effect dominates over probing. This leads to increased linewidths as the quasiprobe moves toward the beam center. In a  $\Pi$ -shaped beam, the passing atoms sense a very rapid increase in laser intensity only at the beam edge and a constant intensity inside the beam. A large variation in laser intensity causes broadening of linewidths and a resultant maximum of linewidths near the beam edge. As atoms move toward the beam center, the constant laser intensity experienced by the atoms and the longer average time of flight inside the  $\Pi$ -shaped beam cause the gradual narrowing of EIA resonances as the atoms move toward the beam center. In other words, the decrease in linewidths upon approaching the beam center for a  $\Pi$ -shaped beam is a typical time-of-flight narrowing.

Radial behavior of EIA amplitudes is notably different for two laser beam shapes at higher laser intensities, as shown in Figs. 7 and 9 for  $1 \text{ mW/cm}^2$ . Amplitudes for the  $\Pi$ -shaped profile do not show large variations along the beam in comparison with the Gaussian profile, where the initial rise in amplitudes turns into a significant and constant decrease. A strong laser intensity near the center of the Gaussian beam, above  $\sim 1 \text{ mW/cm}^2$ , leads to a lower amplitude in comparison to amplitudes farther from the beam center. Similar behavior, a decrease upon approaching the center, becomes present also in  $\Pi$ -shaped beams of a laser intensity higher than  $1 \text{ mW/cm}^2$ . This is attributed to the fact that at high intensities, the laser field dominates over the influence of the magnetic field, so that the effect of the beam profile on the EIA amplitudes becomes less pronounced.

EIA amplitudes and linewidths depend on ambient conditions, stray magnetic field, and room temperature. Effects of stray magnetic field are negligible due to shielding by the triple-layered  $\mu$ -metal cylinder. The variation of room temperature from one set of measurements to the other was within  $\pm 1^\circ\text{C}$ . These temperature variations have a negligible influence on linewidths but may result in changes in EIA amplitudes. Ambient temperature variation shifts the amplitude

radial dependencies, presented in Figs. 6(a) and 7(a), by 10%, preserving their shape.

## V. SUMMARY

We studied Hanle EIA resonances at the  $D_2$  line transition  $F_g = 2 \rightarrow F_e = 3$  in  $^{87}\text{Rb}$  using Gaussian and  $\Pi$ -shaped laser beams with of the same 3-mm radius. We demonstrated that the atom experiences completely different interactions depending on whether traverses one or the other profiled beam. This is shown by the Hanle EIA obtained from transmission of only one cylindrical segment of the entire laser beam. In this way we effectively measured quasiprobe EIA, surrounded by the “pump” beam, that is, by the rest of the laser beam. Since at very low laser intensities, the quasiprobe probes EIA in atoms moving toward the selected region, EIA resonances are narrower in outer regions of the Gaussian beam. At higher laser intensities the quasiprobe can also generate EIA in atoms. Thus, near the center of the Gaussian beam, EIA is widest due to higher power broadening. For a  $\Pi$ -shaped laser beam, the quasiprobe gives the narrowest EIA at the beam center, due to transit-time narrowing of the coherent resonance. EIA amplitudes, in the range of applied laser intensities, are lowest (highest) near the laser beam center for the Gaussian ( $\Pi$ -shaped) profile. Thus, outer regions of the Gaussian beam and central regions of the  $\Pi$ -shaped beam are the most valuable regions in the sense that they contribute the narrowest linewidths and highest amplitudes to the overall EIA. The opposite variation of quasiprobe EIA linewidths with the distance from the laser beam center for the two beam profiles makes the linewidths of whole-beam EIA less dependent on the laser beam profile. Only in the range of laser intensities  $1\text{--}4 \text{ mW/cm}^2$  does the overall EIA with the  $\Pi$ -shaped laser beam have a maximum which exceeds the values obtained with the Gaussian beam that gives a flat intensity dependence.

This work has shown that it is important to take into account the real laser beam profile for proper modeling and analysis of coherent effects in alkali metal vapors. Differences in EIA linewidths obtained using two laser radial beam profiles imply that a theory with assumed  $\Pi$ -shaped radial dependence (common assumption in majority of models) will not produce good agreement with experiments done

usually using a Gaussian or similar beam shape. One practical consequence of these results is that detecting only the wings of the Gaussian laser beam will give narrower EIA resonances than in the case of whole-beam detection.

#### ACKNOWLEDGMENT

This work was supported by the Ministry of Science of the Republic of Serbia, under Grant No. 141003.

- 
- [1] E. Arimondo, *Prog. Opt.* **35**, 257 (1996).  
[2] G. Alzetta, A. Gozzini, L. Moi, and G. Orriolis, *Nuovo Cim.* **36**, 5 (1976).  
[3] S. E. Harris, J. E. Field, and A. Imamoglu, *Phys. Rev. Lett.* **64**, 1107 (1990).  
[4] A. M. Akulshin, S. Barreiro, and A. Lezama, *Phys. Rev. A* **57**, 2996 (1998).  
[5] F. Renzoni, C. Zimmermann, P. Verkerk, and E. Arimondo, *J. Opt. B: Quantum Semiclass. Opt.* **3**, S7 (2001).  
[6] C. Andreeva, S. Cartaleva, Y. Dancheva, V. Biancalana, A. Burchianti, C. Marinelli, E. Mariotti, L. Moi, and K. Nasyrov, *Phys. Rev. A* **66**, 012502 (2002).  
[7] G. Moruzzi and F. Strumia, *The Hanle Effect and Level Crossing Spectroscopy* (Plenum Press, New York, 1991).  
[8] H. Failache, P. Valente, G. Ban, V. Lorent, and A. Lezama, *Phys. Rev. A* **67**, 043810 (2003).  
[9] A. V. Taichenachev, A. M. Tumaikin, and V. I. Yudin, *Phys. Rev. A* **61**, 011802(R) (1999).  
[10] C. Goren, A. D. Wilson-Gordon, M. Rosenbluh, and H. Friedmann, *Phys. Rev. A* **67**, 033807 (2003).  
[11] J. Dalibard and C. Cohen-Tannoudji, *J. Opt. Soc. Am. B* **6**, 2023 (1989).  
[12] A. Javan, O. Kocharovskaya, H. Lee, and M. O. Scully, *Phys. Rev. A* **66**, 013805 (2002).  
[13] C. Y. Ye and A. S. Zibrov, *Phys. Rev. A* **65**, 023806 (2002).  
[14] A. J. Krmpot, M. M. Mijailović, B. M. Panić, D. V. Lukić, A. G. Kovacević, D. V. Pantelić, and B. M. Jelenković, *Opt. Express* **13**, 1448 (2005).  
[15] J. Dimitrijević, D. Arsenović, and B. M. Jelenković, *Phys. Rev. A* **76**, 013836 (2007).  
[16] F. Levi, A. Godone, J. Vanier, S. Micalizio, and G. Modugno, *Eur. Phys. J. D* **12**, 53 (2000).  
[17] A. V. Taichenachev, A. M. Tumaikin, V. I. Yudin, M. Stahler, R. Wynands, J. Kitching, and L. Hollberg, *Phys. Rev. A* **69**, 024501 (2004).  
[18] M. Radonjić, D. Arsenović, Z. Grujić, and B. M. Jelenković, *Phys. Rev. A* **79**, 023805 (2009).  
[19] H. Gilles, B. Cheron, O. Emile, F. Bretenaker, and A. Le Floch, *Phys. Rev. Lett.* **86**, 1175 (2001).  
[20] A. J. Krmpot, S. M. Ćuk, S. N. Nikolić, M. Radonjić, D. G. Slavov, and B. M. Jelenković, *Opt. Express* **17**, 22491 (2009).  
[21] G. Wasik, W. Gawlik, J. Zachorowski, and W. Zawadzki, *Appl. Phys. B* **75**, 613 (2002).  
[22] A. N. Nesmeyanov, *Vapor Pressure of the Chemical Elements*, edited by R. Gray (Elsevier, Amsterdam, 1963).